

Compositional Mapping of the AlGa_N Alloy Composition in Graded Buffer Structures Using Cathodoluminescence

Kagiso Loeto,* Gunnar Kusch, Saptarsi Ghosh, Martin Frentrup, Alexander Hinz, and Rachel Oliver

Herein, the use of cathodoluminescence (CL) hyperspectral mapping in the quantification of the AlGa_N alloy composition in graded buffer structures is explored. The quantification takes advantage of the known parabolic dependence of the AlGa_N bandgap on the alloy composition allowing the AlGa_N near-band-edge (NBE) emission energy recorded from CL to be converted to a composition. The proposed quantification method is first applied to cleaved cross-sections of two nominally step-graded AlGa_N buffer structures each containing five AlGa_N layers with different compositions. By comparing the compositions obtained from CL to those calculated using X-ray diffraction, a close agreement between values from both techniques is observed. However, due to a change in the bowing parameter, some deviation is observed for layers with compositions near 75%. The method is then applied to cleaved cross-sections of an AlGa_N buffer whose group III precursor flow molar ratio is varied linearly throughout the growth. Herein, the hyperspectral nature of the CL datasets is exploited such as to produce composition maps by converting the relevant AlGa_N-NBE emission energy at each pixel of the CL data to a composition.

A key development that has aided in the production of commercially viable AlGa_N/Ga_N power electronic devices is their growth on silicon substrates, known as Ga_N-on-Si. The employment of silicon as a substrate material is advantageous because of the availability of low-cost and large-area wafers of up to 12 inches in diameter, the potential for integration into pre-existing silicon CMOS process lines and silicon's high-thermal conductivity which makes it suitable for high-power operation.^[8,9] With that said, a significant technological challenge for Ga_N-on-Si power electronics is the large ($\approx 54\%$) in-plane thermal expansion coefficient mismatch between Si and Ga_N.^[9] Upon cooling down from growth temperatures, this discontinuity induces large in-plane tensile stresses in Ga_N, which can contribute to cracking of the epilayer, an outcome that is detrimental to device reliability.^[10]

1. Introduction


The AlGa_N/Ga_N semiconductor system has played a crucial role in the success of next-generation low-loss, high-voltage, and high-frequency power electronic devices, such as high-electron-mobility transistors.^[1–6] Compared to their incumbent silicon-based counterparts, AlGa_N/Ga_N-based power electronics provide superior material properties, such as a larger electron saturation velocity, wider electronic bandgap, and higher breakdown fields.^[1,2,4] Moreover, a high mobility and high carrier density 2D electron gas are induced at the AlGa_N/Ga_N interface owing to the materials' inherent polarization and conduction band offset.^[3,7]

To overcome these large tensile stresses, compositionally graded AlGa_N buffer structures can be utilized. The AlGa_N buffer maintains the Ga_N epilayer in a net in-plane compressive strain state at the growth temperature that compensates for the aforementioned tensile stresses upon cool down.^[10,11]

The change in the AlGa_N alloy composition across the depth of the buffer structure is an important factor that governs phenomena such as the strain distribution in the sample and the optical and electrical properties.^[12,13] Thus, it is important to be able to quantify the AlGa_N alloy compositions in these buffer layers. This is especially important in the industrial context for in-line quality control purposes. Quantification can be achieved by employing high-resolution X-ray diffraction (XRD). XRD can directly quantify the AlGa_N compositions within the buffer with a compositional resolution below 1%.^[14] This makes XRD ideal for studying step-graded buffer structures, however, because XRD lacks spatial resolution, it provides only very limited information when being applied to smoothly graded buffer structures.

Energy-dispersive X-ray spectroscopy (EDS) analysis, as applied in electron microscopy, is an alternative technique with spatial resolution that can allow for the compositional mapping of graded AlGa_N buffers. With that said, EDS faces some significant disadvantages. EDS is a relatively insensitive quantification technique whose uncertainty is reliant on effects such as the surface morphology and inhomogeneity of the sample.^[15,16] Moreover, EDS relies on the presence of standards whose

K. Loeto, G. Kusch, S. Ghosh, M. Frentrup, A. Hinz, R. Oliver
Department of Materials Science and Metallurgy
University of Cambridge
Cambridge CB3 0FS, UK
E-mail: kl514@cam.ac.uk

 The ORCID identification number(s) for the author(s) of this article can be found under <https://doi.org/10.1002/pssa.202200830>.

© 2023 The Authors. physica status solidi (a) applications and materials science published by Wiley-VCH GmbH. This is an open access article under the terms of the Creative Commons Attribution License, which permits use, distribution and reproduction in any medium, provided the original work is properly cited.

DOI: 10.1002/pssa.202200830

compositions match that of the sample with standard-less approaches giving relative uncertainties that be as high as 90%.^[17] In addition to the large errors involved, high acceleration voltages are required for the production of characteristic X-rays. This limits the minimum size of the primary electron interaction volume, especially in scanning electron microscopy-based EDS, and hence the lateral spatial resolution.

To overcome the limitations of both XRD and EDS, cathodoluminescence (CL) hyperspectral mapping can be utilized. CL is advantageous as it is a high-throughput technique that provides a nanometre-scale lateral spatial resolution.^[18,19] During CL hyperspectral mapping, a focused electron beam with energy in the kV regime is rastered across the investigated sample surface exciting carriers within the material that can recombine radiatively emitting photons that are then detected. Compositional quantification using CL is not direct but relies on the established relationship between the optical bandgap, obtained as the near-band-edge (NBE) emission energy, and the alloy composition.^[20] The alloy composition can be estimated from the AlGa_N-NBE emission energy using the parabolic composition dependence highlighted by Equation (1).^[13,21] In Equation (1), $E_{g,AlGaN}$, $E_{g,AlN}$, and $E_{g,GaN}$ represent the AlGa_N, AlN, and GaN bandgaps, respectively, x is the AlN fraction and b is the bowing parameter representing the deviation from linearity.

$$E_{g,AlGaN} = E_{g,AlN}(x) + E_{g,GaN}(1 - x) - bx(1 - x) \quad (1)$$

The aim of this work is to explore the possibility of using CL hyperspectral mapping and Equation (1) to quantify the AlGa_N composition in graded buffer structures.

2. Experimental Section

Three multilayered epitaxial AlGa_N buffer structures were investigated and are shown in **Figure 1**. The structures were grown using metalorganic vapour-phase epitaxy (MOVPE) which employed trimethylgallium (TMGa), trimethylaluminium

(TMAl), and ammonia (NH₃) as Ga, Al, and N precursors, respectively. All the samples investigated utilize a silicon (111) substrate and an AlN nucleation layer. The AlGa_N composition in the buffer layers was varied by controlling the group-III precursor flow ratio. The group-III precursor flow molar ratio was abruptly changed to produce the step-graded buffers, as shown in **Figure 1a,b** but was varied linearly throughout for the graded buffer, as shown in **Figure 1c**. The thicknesses shown in **Figure 1** are approximate thicknesses obtained from in situ reflectivity.

The nominally step-graded structures A and B were used to verify the CL-based compositional quantification proposed by comparing to XRD measurements. The AlGa_N compositions for these samples are shown in **Table 1**. After the verification, CL hyperspectral mapping will then be used to quantify the

Table 1. AlGa_N compositions for structures a–c as determined using XRD.

Structure	Layer	AlGa _N composition (%AlN)
Structure A	A1	77
	A2	63
	A3	49
	A4	36
	A5	24
Structure B	B1	78
	B2	70
	B3	56
	B4	51
	B5	38
Structure C	Start composition	75
	End composition	25

Note for structure C only the start and end compositions are shown.

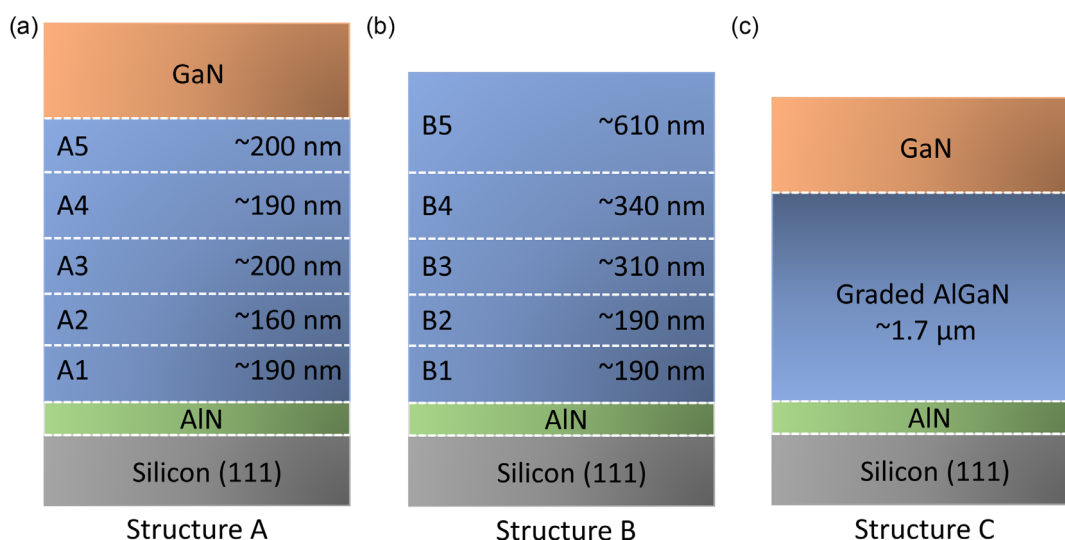


Figure 1. This figure shows the sample structures investigated in this work. a) is structure A, the calibration sample with AlGa_N layers A1–A5. b) is structure B, the test sample with AlGa_N layers B1–B5. c) is structure C, the linearly graded AlGa_N buffer sample. The layer thicknesses shown in the figure are approximate values obtained from in situ reflectivity measurements.

compositional depth profile of structure C. The start and end compositions for structure C are shown in Table 1.

The AlGa_N compositions and associated in-plane strains in these samples were calculated using high-resolution XRD reciprocal space map measurements of the (1-104), (1-105), (2-204), and (2-205) AlGa_N reflections. These measurements were performed with a PANalytical Empyrean diffractometer equipped with a two-bounce hybrid monochromator with 0.25° a primary beam slit, and a PIXcel solid-state area detector.

CL hyperspectral mapping was performed at 10 K and room temperature (RT), on cleaved cross-sections of structures A–C, in an Attolight Allalin 4027 Chronos scanning electron microscope cathodoluminescence system. CL measurements were taken using an iHR320 spectrometer with a grating density of 600 lines per mm. A scan dwell time of 100 ms was utilized for the RT measurements while 50 ms was employed at 10 K. The microscope was operated at an electron beam current of 5 nA and an acceleration voltage of 3 kV, which corresponds to 90% of the beam energy being deposited in a depth of ≈30 nm as determined by Monte-Carlo simulations.^[22] The CL hyperspectral maps were then analyzed using HyperSpy.^[23]

3. Results and Discussion

3.1. Test Samples

To study the depth variation of the AlGa_N alloy composition for an AlGa_N buffer, such as structure C, we first need to verify that indeed CL can be used to quantify the composition in unknown samples. For this, nominally step-graded structures A and B will be utilized. To achieve this verification, the optical bandgaps measured from the AlGa_N NBE emission energy of the AlGa_N layers in each sample will be calculated. The composition will then be estimated from the optical bandgaps using Equation (1) and the 10 K and RT literature values of $E_{g,AlN}$ and $E_{g,GaN}$, which are shown in Table 4, along with the value for b . The compositions calculated from CL will then be compared to those from XRD.

Structure A, shown in Figure 1a, consists of five AlGa_N layers whose composition changes from 78% nearest to the substrate (A1) to 25% furthest from the substrate (A5). In Table 1, there is a large separation in composition between neighboring layers with the minimum difference being 12% between layers A5 and A4.

Cleaved cross-sections of structure A were investigated using CL hyperspectral mapping at RT and 10 K. Secondary electron (SE) images of the cleaved surfaces and corresponding panchromatic CL maps are shown in Figure 2. It should be noted that the regions investigated at 10 K and RT are of different positions on the surface of the sample cross-section. From the SE images shown in Figure 2a,c, the five AlGa_N layers of structure A, labeled A1–A5, can be observed. These layers are especially apparent in the SE image recorded at 10 K which shows a stronger contrast between the layers. Also highlighted in the SE images is the Ga_N epilayer which was grown on top of AlGa_N layer A5.

Figure 2b,d shows the corresponding panchromatic CL intensity maps recorded at 10 K and RT, respectively, for the surfaces in Figure 2a,c. Note that the panchromatic CL maps are not

aligned with the SE images due to drift caused by charging of the sample surface during the acquisition of the CL maps. When compared to that at RT, the panchromatic CL intensity map recorded at 10 K shows a much higher emission intensity and higher signal-to-noise ratio. This is because at 10 K, there is less thermal energy available to activate nonradiative recombination centers. Hence, a larger proportion of nonradiative recombination events are radiative.^[24] From the panchromatic CL maps, it is clear that the layers furthest away from the substrate (A3, A4, and A5) show a higher emission intensity compared to those closer to the substrate (A1 and A2). The lower emission intensity of layers A1 and A2 can be rationalized by an increased density of nonradiative defects, especially threading dislocations, closer to the substrate which limits the optical emission efficiency.^[25] Moreover, the efficiency of the detector decreases as the emission energy tends further into the ultraviolet contributing to the lower observed intensity.

To investigate the luminescence properties of structure A, mean CL spectra were extracted from the hyperspectral datasets corresponding to the fields of view in Figure 2b,d. The approximate regions from which these mean CL spectra were extracted are highlighted by the red boxes in Figure 2a,c. The mean CL spectra are shown in Figure 3a,b for the 10 K and RT data, respectively. The mean spectra show AlGa_N-NBE luminescence bands which correspond to the optical bandgaps of the five layers. For layer A5 in Figure 3a,b, only one AlGa_N-NBE emission band is observed which corresponds to band-to-band recombination within the layer. However, for layers A4 to A1, additional bands are observed because carriers can drift toward neighboring layers with a lower bandgap and recombine. For instance, in Figure 3a, the spectrum for layer A3 at 10 K shows three separate AlGa_N-NBE bands centered at ≈4.03, ≈4.26, and ≈4.54 eV. The band at ≈4.54 eV is the expected emission from this layer whilst those at ≈4.03 and ≈4.26 eV appear due to carrier drift toward layers A4 and A5. A similar rationale applies to the other mean spectra. From this, assuming that no photons from directly excited carriers are recorded from the adjacent layers, it can be said that the AlGa_N-NBE band representing luminescence from the composition of that layer is the one that appears at the highest emission energy in each spectrum. It should be noted that at RT, there is sufficient energy for carriers to escape from localization centers induced by alloy fluctuations.^[26] Hence, diffusion will also contribute to this carrier transfer toward the lower bandgap layers at RT.

Re-examining the RT panchromatic map of structure A in Figure 2d, higher emission intensity regions can be observed for layers A3–A5 that are surrounded by lower emission intensity regions. To unravel the nature of these higher-intensity regions, mean CL spectra were extracted from the regions of lower (1 and 3) and higher (2 and 4) emission intensity highlighted in the RT panchromatic CL map in Figure 2d for layers A4 and A5, respectively. These mean CL spectra are shown in Figure 4a,b. The CL spectra recorded for the lower emission intensity regions (1 and 3) show that AlGa_N-NBE band corresponding to the respective composition of the layers dominates the spectra. For region 3, additional emission bands can be observed at ≈4.1 eV, corresponding to a very localized AlGa_N region of a slightly different composition in layer A4, and at ≈3.9 eV corresponding to drift of carriers toward layer A5. When considering the higher emission intensity regions (2 and 4), a broader and unexpected luminescence band appears at energies in the range ≈3.7–≈4.0 eV and

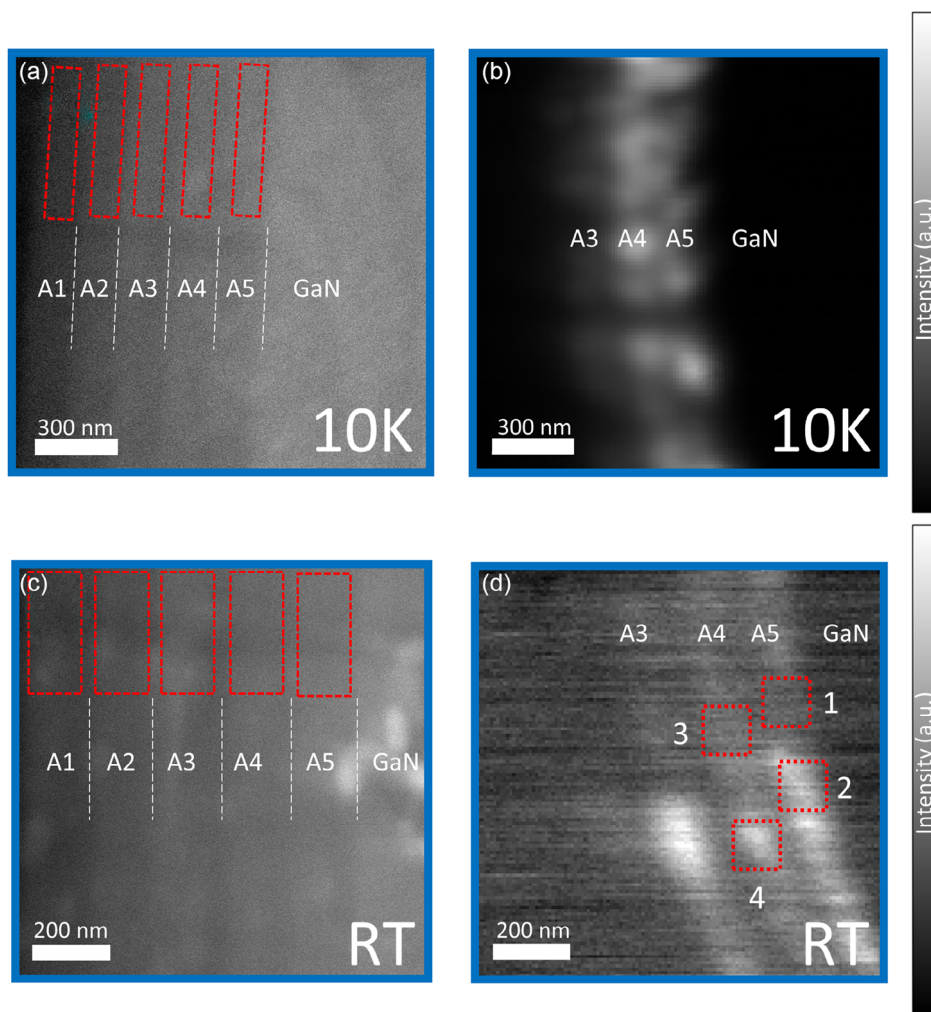


Figure 2. a,c) are secondary electron images recorded at 10 K and RT, respectively, for cleaved cross-sections of structure A. The AlGaIn layers A1–A5 are highlighted in the images. The red boxes in (a,c) represent approximate regions from which mean CL spectra were extracted. b,d) are the corresponding panchromatic CL images for the secondary electron images in (a,c), respectively. The red boxes in (d) represent regions of low emission intensity (1 and 3) and high emission intensity (2 and 4) in which mean spectra were extracted.

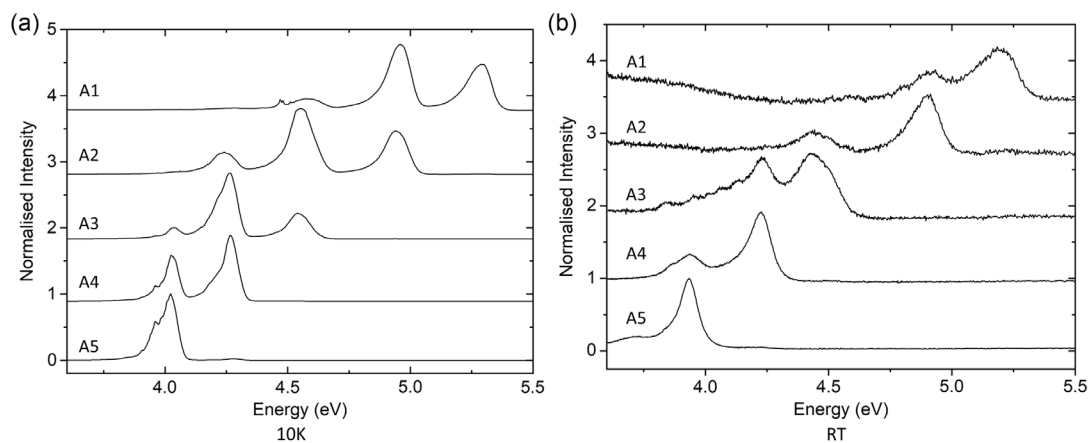


Figure 3. a,b) are the mean CL spectra recorded along the five AlGaIn layers of structure A at 10 K and RT, respectively, and are extracted from the fields of view in Figure 2b,d. The spectra are shifted along the intensity axis for ease of visualization.

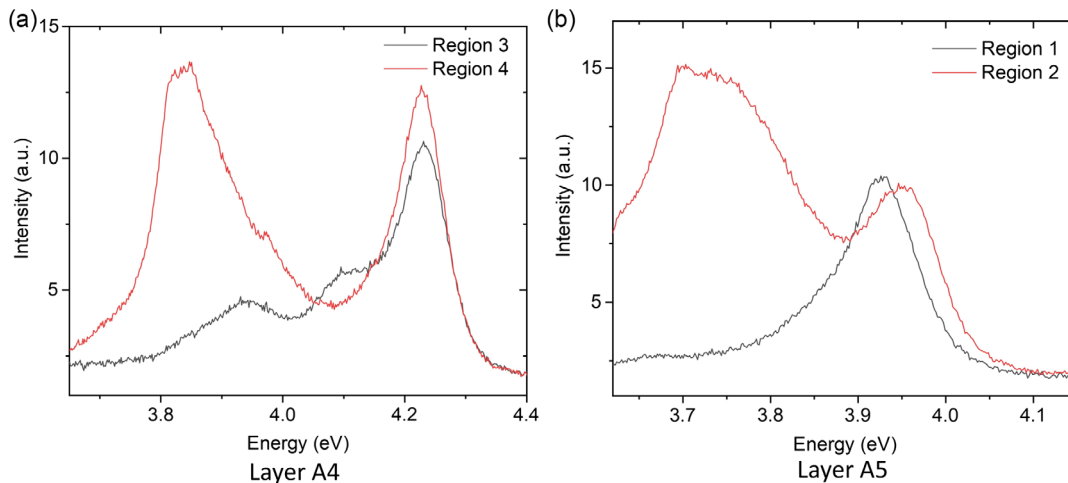


Figure 4. a,b) are RT mean CL spectra for the lower emission intensity regions (1 and 3) and higher emission intensity region (2 and 4) marked in Figure 2d.

dominates the luminescence intensity. This emission band only manifests when similar higher-intensity regions are probed at RT and always appears in the same emission energy range. In fact, this RT trend is consistent for all the samples investigated in this work. The luminescence from these regions is associated with AlGaIn regions within the layers that likely expose different crystallographic facets with a lower incorporation rate of AlN and hence lower emission energy than the surrounding AlGaIn matrix.^[27] In the analysis that follow, these high-emission intensity regions will be disregarded and only mentioned briefly as they are beyond the scope of this work and do not affect the analysis.

Structure B also consists of five AlGaIn layers whose composition changes from 78% nearest to the substrate (B1) to 38% furthest from the substrate (B5). Compared to structure A, the minimum separation between compositions in neighboring layers is 5% between layers B3 and B4. Cleaved cross-sections of structure B were investigated using CL hyperspectral mapping at RT and 10 K. SE images of the cleaved surfaces are shown in Figure 5a,c for the 10 K and RT data, respectively. The corresponding panchromatic CL maps of this sample are shown in Figure 5b, d. Similarly to structure A, only the layers furthest from the substrate (B3–B5) can be observed from the panchromatic CL maps.

Mean CL spectra were extracted along the lengths of the AlGaIn layers in the CL hyperspectral maps for the fields of view in Figure 5. The approximate regions from which these mean CL spectra were extracted are highlighted by the red boxes in Figure 5a,c. The mean spectra are shown in Figure 6 for the 10 K and RT datasets. As shown in Figure 6, the highest energy AlGaIn-NBE bands for each spectrum can be observed which were established to correspond to the AlGaIn composition of that layer. However, for layer B2 at 10 K, the highest energy band observed is that from layer B1 which can be observed at ≈ 5.3 eV. Even though it was ensured that the boundaries of the region in which the mean spectrum of layer B2 was collected did not encroach into layer B1, the finite size of the interaction volume, which was estimated to be ≈ 30 nm from Monte-Carlo simulations,^[22] resulted in photons emitted from layer B1 being

collected. With that being said, CL was able to distinguish between layers B1 and B2 which have measured thicknesses of ≈ 190 nm highlighting the few 10 nm scale spatial resolutions of this technique. This is especially apparent at RT where no emission from layer B1 can be observed in the mean spectrum extracted from B2. Similar to structure A, luminescence peaks associated with the higher emission intensity regions observed in Figure 5b can be seen in Figure 6b. These appear in the range ≈ 3.7 – ≈ 4.0 eV for layers B2–B5 in the RT spectra. An observation to note in Figure 6a is the closeness of emission energies between the compositions of layers B3 and B4. This is exemplified by the spectrum extracted for layer B3 where the emission from the composition of this layer appears as a shoulder on the emission associated with diffusion toward layer B4. The closeness of the emission energies of these layers suggests a closeness in the AlGaIn alloy compositions that can nonetheless be resolved using CL.

To quantify the AlGaIn alloy compositions for the layers in structures A and B, Gaussian curves were fitted to the AlGaIn-NBE bands for the spectra in Figure 3 and 6. The center emission energy was then extracted from the fit for the band that is associated with emission from the alloy composition of that layer. These center emission energies were then converted to a composition using Equation (1) by employing the materials parameters, as shown in Table 4. The calculated AlGaIn compositions for each layer in structures A and B are shown in Table 3 along with the corresponding compositions calculated from XRD. The error in the AlGaIn composition calculated from CL represents the uncertainty in the CL center emission energy obtained from the fit and the uncertainty in the CL emission energy as induced by changes the in-plane strain within the layers. To calculate the error associated with changes the in-plane strain, layers A1 and A5 were considered. These have the largest measured difference in in-plane strain being a tensile strain of 0.0001 and a compressive strain of 0.0021, respectively, giving an in-plane strain difference ($\Delta\epsilon$) of 0.0022. Equation (2), derived by Lee et al.,^[28] shows the relationship between the bandgap emission energy and in-plane stress in GaN. This was used to estimate the maximum change in the bandgap energy (ΔE_{CL}) produced by the

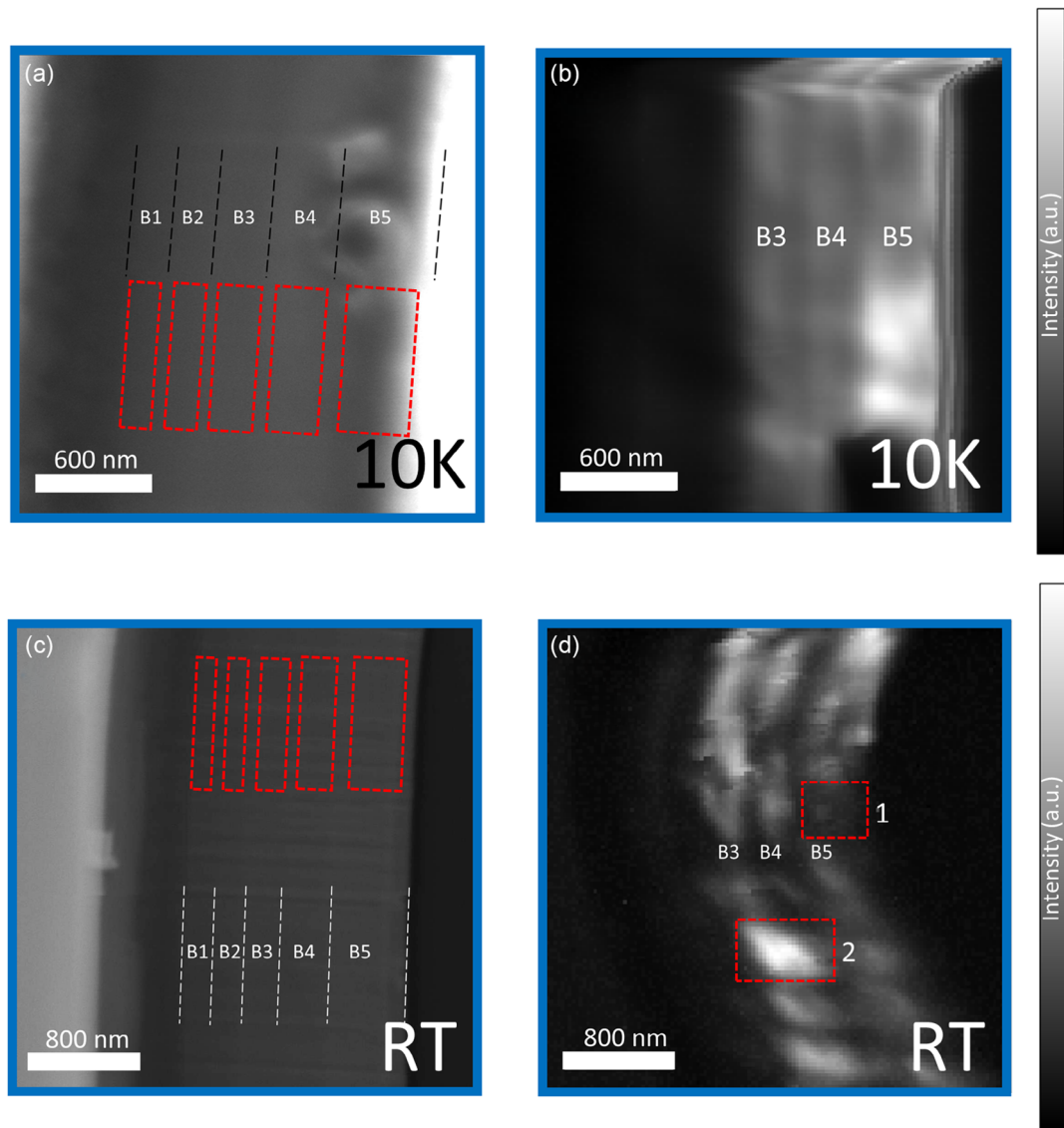


Figure 5. a,c) are secondary electron images recorded at 10 K and RT, respectively, for cleaved cross-sections of structure B. The AlGaIn layers B1–B5 are highlighted in the images. The red boxes in (a,c) represent approximate regions from which mean CL spectra were extracted. b,d) are panchromatic CL images recorded at 10 K and RT, respectively, from cleaved cross-sections of structure B. The red boxes in (b,d) represent regions of lower (1) and higher (2) emission intensity.

stress difference ($\Delta\sigma$) by assuming that the stress in the AlGaIn layers is comparable to that in the GaN layer similar to.^[20] The stress difference was calculated from the strain difference using Equation (3). The elastic constants C11, C12, C13, and C33 for the A1 and A5 AlGaIn layers were calculated as a weighted average from those of GaN and AlN, as shown in Table 2.

$$\Delta E_{CL} = \Delta\sigma \times 42 \text{meV.GPa}^{-1} \quad (2)$$

$$\Delta\sigma = \Delta\varepsilon \left(C11 + C12 - 2 \times \frac{C13^2}{C33} \right) \quad (3)$$

There is a close agreement between the CL and XRD compositions, especially for the last four layers grown (A2–A5 and

B2–B5) with no discernible difference between the RT and 10 K data. For the first AlGaIn layers grown (A1 and B1), the method shows a larger deviation between the compositions determined from CL with those from XRD. In fact, this deviation is observed to increase from minimum in the last layers grown (A5 and B5) to maximum for the first layers grown (A1–B1). Rationale for this deviation can be attributed to the calculation of the composition using Equation (1). First, the calculation relies on using the literature values of the bowing parameter. In this case, it was assumed to be 0.9 eV^[29] and consistent between the different AlGaIn layers of structures A and B. However, in the literature, there are disagreements in the value of the bowing parameter with a range of values being reported.^[30,31] Berrah et al.^[32] have reported a dependence of the bowing parameter

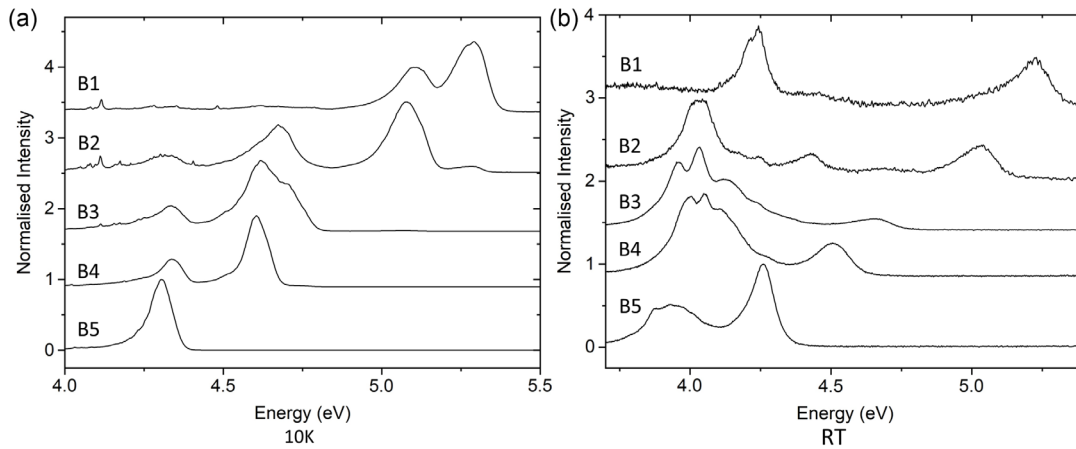


Figure 6. a,b) are the mean CL spectra recorded along the five AlGaIn layers of structure B at 10 K and RT, respectively, from the fields of view in Figure 5c,d. The spectra are shifted along the intensity axis for ease of visualization.

Table 2. Elastic constants C11, C12, C13, and C33 for GaN and AlN taken from Ref. [37].

Elastic constant	GaN [GPa]	AlN [GPa]
C11	390	396
C12	145	137
C13	106	108
C33	398	373

Table 3. AlGaIn alloy compositions calculated for structures A and B using CL compared to values determined from XRD measurements.

Layer ^{a)}	AlGaIn comp. (% AlN)			In-plane strain
	CL at RT	CL at 10 K	XRD	
A5	25 ± 3	25 ± 3	24	-0.0021
A4	37 ± 3	35 ± 3	36	-0.0020
A3	45 ± 3	46 ± 3	49	-0.0020
A2	58 ± 3	60 ± 3	63	-0.0014
A1	70 ± 3	71 ± 3	77	+0.0001
B5	38 ± 3	37 ± 3	38	-0.0006
B4	48 ± 3	48 ± 3	51	-0.0004
B3	53 ± 3	53 ± 3	56	-0.0011
B2	65 ± 3	64 ± 3	70	-0.0008
B1	71 ± 3	71 ± 3	78	-0.0003

^{a)}The strain values determined from XRD are also shown.

on the AlGaIn alloy composition determining values similar to the 0.9 eV used earlier for compositions in the 25%–50% range but ≈ 1.3 eV for compositions close to 75%. As an illustration, applying this larger bowing parameter to the RT data for layers A1 and B1 produces the values 73% and 74%, respectively, which are much closer to the 78% calculated from XRD. Furthermore, the bowing parameter will depend on the in-plane strain state^[33] which was observed to vary across the layers, as seen in Table 3.

Second, in the calculation for the composition performed, there is an assumption that the AlGaIn-NBE emission energy calculated corresponds to the bandgap of the AlGaIn. However, effects like localized heating by the electron beam and Stokes's shift will lead to a deviation between these two quantities.^[33,34]

With that said, in general, there is a close agreement between the AlGaIn compositions calculated from CL with those from XRD. Deviations observed at higher AlGaIn alloy compositions can be corrected by considering changes in the bowing parameter. As such, this method can be used to quantify AlGaIn alloy compositions in graded buffers.

3.2. Depth-Resolved Analysis of Structure C

The above analysis has verified that CL can be applied in the quantification of alloy compositions in unknown step-graded AlGaIn buffer structures. The next step will be to apply this method to structure C. Figure 7a,b are panchromatic CL maps recorded for cross-sections of structure C at 10 K and RT, respectively. The majority of the fields of view is occupied by the graded AlGaIn layer with the regions occupied by the AlN and GaN layers being labeled in the figures. Similar to the previous samples, higher emission intensity regions can be observed in the RT panchromatic map, as shown in Figure 7b.

From the CL hyperspectral maps of which the panchromatic images were extracted, Gaussian curves were fitted to the spectrum in each pixel. At 10 K only one Gaussian curve was utilized to fit the single AlGaIn-NBE emission peak observed at each pixel. This peak shifted according to the AlGaIn composition at that pixel from ≈ 4.0 to ≈ 5.4 eV. At RT, an additional Gaussian was added to account for the higher emission intensity regions which emit in the range ≈ 3.7 to ≈ 4.0 eV. The center emission energy was extracted from the Gaussian associated with the AlGaIn composition at each pixel and converted to a composition using Equation (1) and the materials parameters in Table 4. This allowed the AlGaIn composition to be mapped across cross-sections of structure C. These composition maps are shown in Figure 7c,d for the 10 K and RT datasets. It is noted here that carriers will drift toward the lower bandgap AlGaIn as discussed

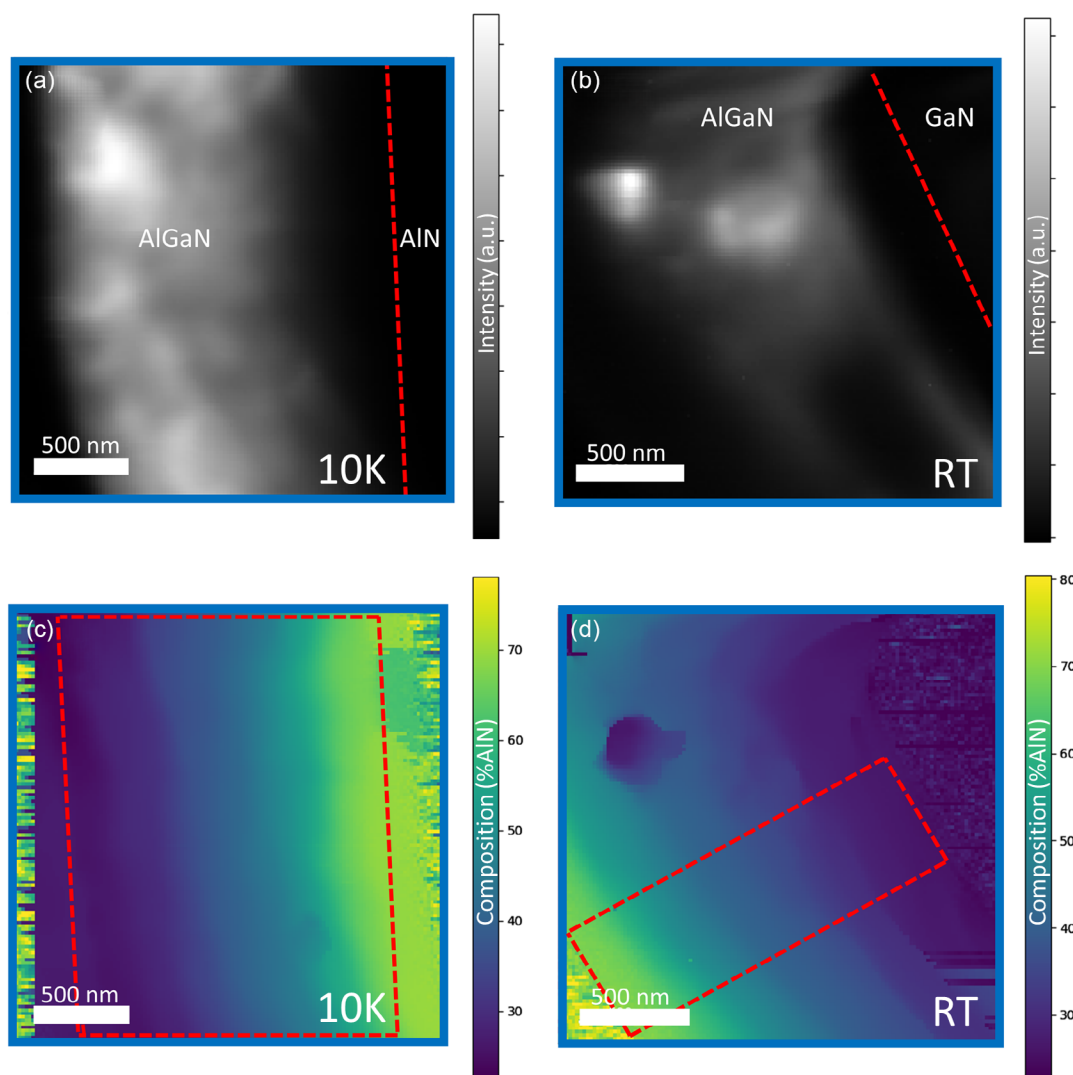


Figure 7. a,b) show the panchromatic CL maps recorded from cross-sections of structure C at 10 K and RT, respectively. Highlighted in the figures are the AlGaIn and AlIn regions. c,d) show the compositional variation of the AlGaIn alloy composition at 10 K and RT. Line scans were extracted from the marked rectangular regions.

Table 4. Values of $E_{g,AlIn}$ and $E_{g,GaN}$ at 10 K and RT and the bowing parameter, b , used to calculate the AlGaIn compositions from the CL optical bandgap.

Quantity	Value at 10 K	Value at RT
$E_{g,AlIn}$	6.28 eV ^[38]	6.20 eV ^[39]
$E_{g,GaN}$	3.47 eV ^[40]	3.39 eV ^[41]
b	0.9 eV ^[29]	

earlier in the text. Hence, there will be emissions from these lower bandgap regions being detected along with that from the AlGaIn region being probed directly by the electron beam.

To investigate the change in the AlGaIn composition across structure C, linescans were extracted as an average over the regions highlighted in Figure 7c,d. These regions approximately

cover the full extent of the depth of the AlGaIn buffer. **Figure 8** shows these linescans along with a linear trend-line suggested by the group-III precursor flow ratio. The start and end gas-phase AlGaIn compositions of the linear trend were determined to be $\approx 7.5\%$ and $\approx 25\%$ from the precursor flow rates in the growth recipes. Compared to the gas-phase composition in the reactor during growth, the start and end compositions obtained from the CL linescans show good agreement being $69\% \pm 3\%$ and $25\% \pm 3\%$, respectively, and at both measurement temperatures. As detailed above, the deviation observed at high compositions is related to a change in the bowing parameter.

Compared to the linear trend-line, the depth variation of the composition obtained from CL is sublinear at both measurement temperatures. This behavior is expected since the species obtained from pyrolysis of TMAI are reactive and undergo parasitic pre-reactions slowing down the effective growth rate of the AlGaIn layer and reducing the incorporation efficiency of AlN

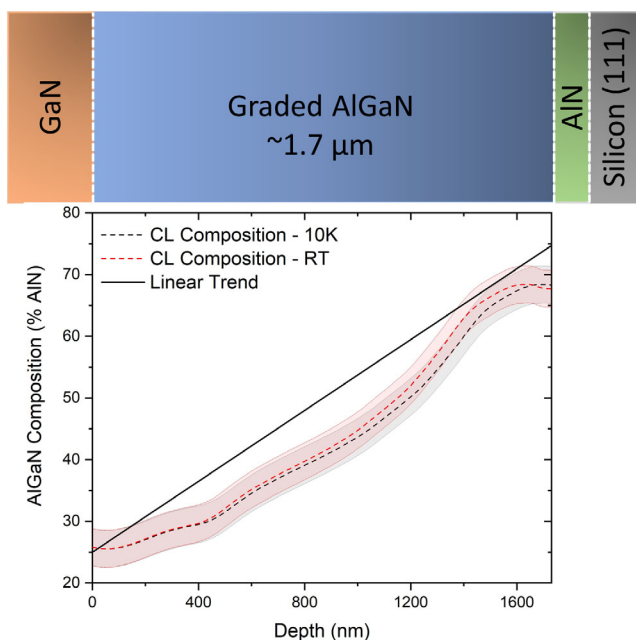


Figure 8. This figure shows the depth-variations in the AlGaIn alloy composition obtained from CL at 10 K and RT. Also included is linear trend-line as suggested by the input group III precursor flow ratio into the reactor.

leading to a lower AlGaIn composition when compared to the composition that would be suggested by the input group III precursor flow ratio into the reactor.^[35,36]

4. Conclusion

CL hyperspectral mapping was used to quantify the AlGaIn alloy composition in graded buffer structures at 10 K and RT. This was done by converting the AlGaIn-NBE center emission energy from CL to a composition using the parabolic relationship relating the two quantities. First, cleaved cross-sections of two AlGaIn buffer structures, each with five AlGaIn layers of different compositions, were considered. From CL panchromatic maps, higher intensity regions were observed at RT which emitted in the ≈ 3.7 – ≈ 4.0 eV regime. These local variations in the AlGaIn composition within the layers could be observed due to the high spatial resolution of CL. Similarly, other local variations such as those relating to defects, surface morphology changes, and other deviations from the intended growth process can also potentially be resolved using CL. Utilizing the hyperspectral datasets, mean spectra were extracted along the lengths of the AlGaIn layers within the buffer structures and by extracting the center emission energy from the relevant AlGaIn-NBE bands, estimates of the compositions of the layers could be calculated. Comparisons of the compositions from the CL analysis with those determined from XRD showed a close match. However, a deviation was observed for the first layer grown in each sample corresponding to the layer with the highest composition. A change in the bowing parameter at such compositions was used to rationalize this deviation. The quantification was then applied to cleaved cross-sections of an AlGaIn buffer whose group-III precursor flow

molar ratio was varied linearly throughout the growth. From the CL hyperspectral datasets, the center emission energy at each pixel was converted to a composition producing compositional maps such that the change in composition with depth could be extracted. The depth-variation in AlGaIn alloy composition obtained from CL was sublinear when compared to the linear trend expected from the group-III precursor flow ratio in the MOVPE reactor during the growth process. This was rationalized by parasitic pre-reactions of the TMAI precursor species which reduced the incorporation rate of AlN. The close agreement between CL and XRD and the application of this technique to buffers whose group-III precursor flow molar ratio were varied linearly during growth demonstrates its potential as a quality control tool for industrial semiconductor fabrication processes.

Acknowledgements

The materials studied in this work were grown using the Engineering and Physical Sciences Research Council (EPSRC) grants, National Epitaxy Facility grant (EP/N017927/1) and InGaNET, “Integration of RF Circuits with High Speed GaN Switching on Silicon Substrates” grants (EP/N017927/1) and (EP/N014820/2). This research was supported by EPSRC Cambridge NanoDTC, EP/S022953/1. Alexander Hinz would like to acknowledge funding for his position in the framework of a Research Fellowship by the Deutsche Forschungsgemeinschaft (DFG) under the grant number HI 2141/1-1. Kagiso Loeto would like to acknowledge the Botswana government for his PhD funding. Dr. Christian Monachon of AttoLight is thanked for his ongoing support of the CL system.

Conflict of Interest

The authors declare no conflict of interest.

Data Availability Statement

The data that support the findings of this study are available from the corresponding author upon reasonable request.

Keywords

AlGaIn buffer structures, cathodoluminescence, high-electron-mobility transistors, III-nitrides

Received: November 28, 2022

Revised: January 24, 2023

Published online: April 5, 2023

- [1] R. Pengelly, S. Wood, J. Milligan, S. Sheppard, W. Pribble, *IEEE Trans. Microwave Theory Techn.* **2012**, *60*, 1764.
- [2] M. Ishida, T. Ueda, T. Tanaka, D. Ueda, *IEEE Trans. Electron Devices* **2013**, *60*, 3053.
- [3] M. Kuzuhara, J. T. Asubar, H. Tokuda, *Jpn. J. Appl. Phys.* **2016**, *55*, 070101.
- [4] H.-P. Lee, J. Perozek, L. D. Rosario, C. Bayram, *Sci. Rep.* **2016**, *6*, 37588.
- [5] S.-H. Baek, G.-W. Lee, C.-Y. Cho, S.-N. Lee, *Sci. Rep.* **2021**, *11*, 7172.
- [6] B. J. Baliga, *Semicond. Sci. Technol.* **2013**, *28*, 074011.

- [7] O. Ambacher, J. Smart, J. R. Shealy, N. G. Weimann, K. Chu, M. Murphy, W. J. Schaff, L. F. Eastman, R. Dimitrov, L. Wittmer, M. Stutzmann, W. Rieger, J. Hilsenbeck, *J. Appl. Phys.* **1999**, *85*, 3222.
- [8] S. Yang, Q. Jiang, B. Li, Z. Tang, K. J. Chen, *Phys. Status Solidi C* **2014**, *11*, 949.
- [9] Y. Zhong, J. Zhang, S. Wu, L. Jia, X. Yang, Y. Liu, Y. Zhang, Q. Sun, *Fundam. Res.* **2022**, *2*, 462.
- [10] H. F. Liu, S. B. Dolmanan, L. Zhang, S. J. Chua, D. Z. Chi, M. Heuken, S. Tripathy, *J. Appl. Phys.* **2013**, *113*, 023510.
- [11] X. He, Y. Feng, X. Yang, S. Wu, Z. Cai, J. Wei, J. Shen, H. Huang, D. Liu, Z. Chen, C. Ma, W. Ge, B. Shen, *Appl. Phys. Express* **2021**, *15*, 011001.
- [12] Y. Yang, P. Xiang, M. Liu, W. Chen, Z. He, X. Han, Y. Ni, F. Yang, Y. Yao, Z. Wu, Y. Liu, B. Zhang, *J. Cryst. Growth* **2013**, *376*, 23.
- [13] S. R. Lee, A. F. Wright, M. H. Crawford, G. A. Petersen, J. Han, R. M. Biefeld, *Appl. Phys. Lett.* **1999**, *74*, 3344.
- [14] J. A. Newman, P. D. Schmitt, S. J. Toth, F. Deng, S. Zhang, G. J. Simpson, *Anal. Chem.* **2015**, *87*, 10950.
- [15] S. Nasrazadani, S. Hassani, *Handbook of Materials Failure Analysis with Case Studies From the Oil and Gas Industry* (Eds: A. S. H. Makhlof, M. Aliofkhaezai), Butterworth-Heinemann, Oxford **2016**, pp. 39–54.
- [16] W. J. Wolfgang, *Handbook of Materials Failure Analysis with Case Studies from the Aerospace and Automotive Industries* (Eds: A. S. H. Makhlof, M. Aliofkhaezai), Butterworth-Heinemann, Boston **2016**, pp. 279–307.
- [17] D. E. Newbury, C. R. Swyt, R. L. Myklebust, *Anal. Chem.* **1995**, *67*, 1866.
- [18] P. R. Edwards, L. K. Jagadamma, J. Bruckbauer, C. Liu, P. Shields, D. Allsopp, T. Wang, R. W. Martin, *Microsc. Microanal.* **2012**, *18*, 1212.
- [19] M. Merano, S. Sonderegger, A. Crottini, S. Collin, P. Renucci, E. Pelucchi, A. Malko, M. H. Baier, E. Kapon, B. Deveaud, J.-D. Ganière, *Nature* **2005**, *438*, 479.
- [20] I.-H. Lee, Y. Park, *Phys. Status Solidi A* **2002**, *192*, 67.
- [21] M. Cardona, *Phys. Rev.* **1963**, *129*, 69.
- [22] D. Drouin, A. R. Couture, D. Joly, X. Tastet, V. Aimez, R. Gauvin, *Scanning* **2007**, *29*, 92.
- [23] F. D. L. Peña, V. T. Fauske, P. Burdet, E. Prestat, P. Jokubauskas, M. Nord, T. Ostasevicius, K. E. MacArthur, M. Sarahan, D. N. Johnstone, J. Taillon, A. Eljarrat, V. Migunov, J. Caron, T. Furnival, S. Mazzucco, T. Aarholt, M. Walls, T. Slater, F. Winkler, B. Martineau, G. Donval, R. McLeod, E. R. Hoglund, I. Alkneit, I. Hjorth, T. Henninen, L. F. Zagonel, A. Garmannslund, A. Skorikov, hyperspy/hyperspy: HyperSpy v1.5.2, **2018**.
- [24] U. Jahn, J. Menniger, R. Hey, H. T. Grahn, *Appl. Phys. Lett.* **1994**, *64*, 2382.
- [25] M. Albrecht, J. Weyher, B. Lucznik, I. Grzegory, S. Porowski, *Appl. Phys. Lett.* **2008**, *92*, 231909.
- [26] A. A. Roble, S. K. Patra, F. Massabuau, M. Frentrup, M. A. Leontiadou, P. Dawson, M. J. Kappers, R. A. Oliver, D. M. Graham, S. Schulz, *Sci. Rep.* **2019**, *9*, 18862.
- [27] B. Neuschl, K. J. Fujan, M. Feneberg, I. Tischer, K. Thonke, K. Forghani, M. Klein, F. Scholz, *Appl. Phys. Lett.* **2010**, *97*, 192108.
- [28] I.-H. Lee, I.-H. Choi, C. R. Lee, S. K. Noh, *Appl. Phys. Lett.* **1997**, *71*, 1359.
- [29] A. Goyal, A. K. Kapoor, R. Raman, S. Dalal, P. Mohan, R. Muralidharan, *J. Appl. Phys.* **2015**, *117*, 225702.
- [30] F. Yun, M. A. Reshchikov, L. He, T. King, H. Morkoç, S. W. Novak, L. Wei, *J. Appl. Phys.* **2002**, *92*, 4837.
- [31] O. Katz, B. Meyler, U. Tisch, J. Salzman, *Phys. Status Solidi A* **2001**, *188*, 789.
- [32] S. Berrah, B. Abdelkader, A. Hamza, *Semicond. Phys. Quantum Electron. Optoelectron.* **2008**, *20*, 71.
- [33] G. Orsal, Y. El Gmili, N. Fressengeas, J. Streque, R. Djerboub, T. Moudakir, S. Sundaram, A. Ougazzaden, J. Salvestrini, *Opt. Mater. Express* **2014**, *4*, 1030.
- [34] C. Gaw, V. Swaminathan, *Mater. Lett.* **1985**, *3*, 145.
- [35] A. Gundimeda, M. Rostami, M. Frentrup, A. Hinz, M. J. Kappers, D. J. Wallis, R. A. Oliver, *J. Phys. D: Appl. Phys.* **2022**, *55*, 175110.
- [36] J. Stellmach, M. Pristovsek, Ö. Savas, J. Schlegel, E. Yakovlev, M. Kneissl, in *15th Int. Conf. on Metalorganic Vapor Phase Epitaxy (ICMOVPE-XV)*, Vol. 315, Incline Village, Nevada, United States **2011**, pp. 229–232.
- [37] I. Vurgaftman, J. R. Meyer, *J. Appl. Phys.* **2003**, *94*, 3675.
- [38] I. H. Nwigboji, J. I. Ejembi, Y. Malozovsky, B. Khamala, L. Franklin, G. Zhao, C. E. Ekuma, D. Bagayoko, *Mater. Chem. Phys.* **2015**, *157*, 80.
- [39] H. Yamashita, K. Fukui, S. Misawa, S. Yoshida, *J. Appl. Phys.* **1979**, *50*, 896.
- [40] J.-H. Ryou, W. Lee, in *Nitride Semiconductor Light-Emitting Diodes (LEDs)* (Eds: J. Huang, H.-C. Kuo, S.-C. Shen), 2nd ed., Woodhead Publishing Series in Electronic and Optical Materials, Woodhead Publishing, Sawston **2018**, pp. 43–78.
- [41] S. Strite, H. Morkoç, *J. Vac. Sci. Technol., B: Microelectron.* **1992**, *10*, 1237.